Localization physics in graphene moiré superlattices

Chandan Kumar, Saurabh Kumar Srivastav, Priyo Adhikary, Sumilan Banerjee, Tanmoy Das, and Anindya Das[*]

Department of Physics, Indian Institute of Science, Bangalore 560 012, India

Since the discovery of graphene, the localization physics has been studied extensively, and both weak antilocalization (WAL) and weak localization (WL) have been observed. A graphene superlattice (GSL) with multiple Dirac cones has emerged as a focus point in condensed-matter physics in recent years. However, the localization physics at multiple Dirac cones has not been studied to date. Here, we study the magnetoconductance in hexagonal boron nitride-graphene moiré-superlattice devices. Our magnetoconductance results show a clear signature of WL at the cloned Dirac cone (CDC) over one decade of variation of both carrier concentration and temperature in the two devices. In contrast, the WAL becomes stronger at the primary Dirac cone (PDC) with increasing temperature and lower carrier concentration in one device, in agreement with previous studies, whereas the other device shows stronger WAL for both lower temperature and carrier concentration. Since the observation of WAL at PDC is expected in a cleaner device due to the π Berry phase, it is natural to ask whether the observation of WL at CDC in our GSL devices has any connection to Berry phase change or not. In order to address this issue we measure the Shubnikov–de Haas (SdH) resistance oscillations, which show a shift of the Berry phase by π from PDC to CDC, indicating the role of the Berry phase for observing WL at CDC. We further corroborate our results with realistic electronic band structure calculations, which suggest a change in the Fermi surface topology from that with a small Fermi pocket enclosing a single PDC in each valley to a large Fermi surface shared by all the CDCs, in accordance with the change in oscillation frequency from PDC to CDC in the SdH measurements.

I. INTRODUCTION

The correlations between electron wave functions lead to quantum interference corrections to Drude-Boltzmann conductivity [1,2]. An electron traversing through a diffusive system gets scattered by impurities in all possible directions, and electron trajectories form a close loop after multiple scattering. The difference in phase acquired by the electronic wave functions in such close loops, often described by time-reversal paths, is zero, leading to enhanced backscattering and thereby a decrease in conductance. This phenomenon is referred to as weak localization (WL) [3]. However, it is realized that if the spin-orbit interaction (SOI) of the system is sufficiently large, the quantum interference results in an increase of conductance, a phenomenon known as weak antilocalization (WAL) [4–7]. Regimes of WL and WAL are sensitive to different types of symmetry breaking as well as scattering mechanisms in conventional two-dimensional systems and have been studied extensively [5–9].

The physics of localization in graphene is much richer due to its relativistic nature. The low-energy excitation in graphene is described by relativistic Dirac spinors with two-component pseudospin. This additional pseudospin quantum number gives rise to π and 2π Berry phases in graphene and bilayer graphene, respectively [10]. The Berry phase adds an additional phase correction to the quantum interference, and it has been predicted theoretically that the graphene and

bilayer graphene would manifest WAL and WL, respectively [10–16]. However, experimentally in graphene itself both WL [17–33] and WAL [20,34–36] have been reported. The interplay between WL and WAL in graphene relies on the relative strength of different symmetry-breaking processes [12,14,15,17,27,30,33,35,37,38]. In a clean graphene device WAL will dominate at the Dirac point, whereas the presence of strong intervalley scattering will restore WL. Thus, the physics of localization in graphene is very intricate and depends on the type of scatterers [12,13,16,17,39], which varies from device to device. The graphene superlattice (GSL) is an ideal platform to study the effect of Berry phase on localization physics for the following reasons. In the GSL the extra set of Dirac cones known as cloned Dirac cones appears symmetrically around the primary Dirac cone. Very recently, it was shown experimentally [40] that the Berry phase changes from π to 2π (or zero) from the primary Dirac cone (PDC) to the cloned Dirac cone (CDC). Motivated by this Berry phase transition [40,41], we have carried out magnetoconductance (MC) studies on two GSL devices with multiple Dirac cones. The GSL devices are created using the heterostructure of hexagonal boron nitride (hBN) and graphene, where the small angle mismatch between the crystallographic planes of graphene and hBN generates a weak periodic moiré potential. The MC studies at small magnetic fields at different carrier concentrations, n and temperatures, T show positive MC around the CDC in both the devices, suggesting a clear signature of WL. In contrast, the MC curve at small magnetic fields around the PDC is negative for lower carrier concentration and higher temperature in one device, which is consistent
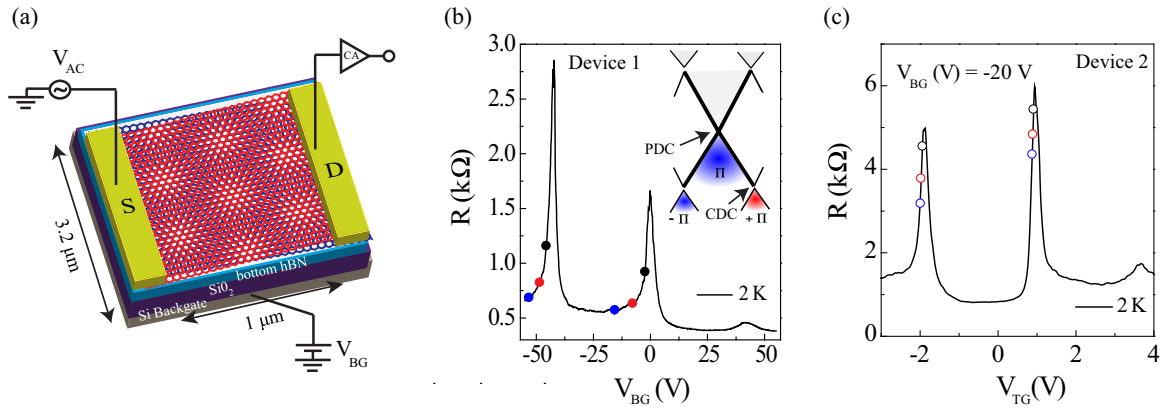
_____
[*]anindya@iisc.ac.in

FIG. 1. (a) Schematic of the device with the moiré superlattice potential created by hBN. (b) The resistance as a function of the back-gate voltage for device 1 at 2 K and zero magnetic field. The black, red, and blue solid circles around CDC and PDC represent densities of 1×10^{11}, 5×10^{11}, and 1×10^{12} cm^{-2} with respect to CDC and PDC, respectively. The inset shows the theoretically computed band dispersion of the graphene moiré superlattice. The Berry phase around a PDC is π. Although the Berry phase around the individual CDC points is π with the opposite sign, the total Berry phase for the electrons enclosing the entire superlattice Brillouin zone is zero. (c) The resistance as a function of the top-gate voltage for device 2 at 2 K and zero magnetic field for $V_{BG} = -20$ V. The black, red, and blue open circles around CDC and PDC represent densities of 6×10^{10}, 8×10^{10}, and 1×10^{11} cm^{-2} with respect to CDC and PDC, respectively.

with the literature [20]. However, in the other device MC is negative at both lower carrier concentration and temperature. The predominantly observed negative MC at the PDC in both the GSL devices in a certain range of carrier concentration and temperature suggests the signature of WAL, which is expected in cleaner graphene devices (hBN-graphene-hBN) due to the π Berry phase. Thus, the observation of WL around the CDC in the same GSL device may suggest some connection with the Berry phase. One of the possible explanations could be the shift of the Berry phase from π to 2π (or zero) from the PDC to CDC as predicted [41]. Thus, we have further carried out Shubnikov–de Haas (SdH) quantum oscillation measurements as a function of magnetic field in our GSL device, which clearly shows the shift of Berry phase by π from the PDC to CDC. The shift of Berry phase from the PDC to CDC is supported by our realistic tight-binding band structure calculations, which also indicate a small Fermi pocket around each PDC in the Brillouin zone (BZ) and a large Fermi surface surrounding all the CDCs for the carrier densities accessible in the experiment near the Dirac points. The change in Fermi surface topology from small pockets to a large Fermi surface is in direct agreement with our measured Fermi surface from the SdH oscillation frequency, which shows that the size of the Fermi surface near the CDC is four to five times higher than the expected Fermi surface enclosing a single CDC. The three experimental observations (localization, Berry phase shift, and SdH oscillation frequency) together with the theoretical calculations help us to uncover the intricate interplay of the Berry phase and localization physics in GSL devices.

II. DEVICE FABRICATION AND CHARACTERIZATION

The GSL heterostructures are prepared by making a stack of hBN/graphene/hBN using the pickup technique [42]. First, a glass slide is prepared with a layer of Polydimethylsiloxane (PDMS) and Ploy-propylene carbonate (PPC). This glass

slide is used to pick up hBN and graphene flakes, which were exfoliated separately on different SiO$_2$ substrates. The glass slide containing the hBN/graphene stack is then aligned and transferred to another hBN layer, which was exfoliated on a new SiO$_2$ substrate. The finally prepared stack of hBN/graphene/hBN is then cleaned with chloroform, acetone, and isopropyl alcohol (IPA). This is followed by standard lithography to define the contacts. The devices are developed and ion etched in a CHF$_3$ and O$_2$ environment just before Cr (5 nm)/Au (70 nm) evaporation at a base pressure of 10^{-7} mbar. With this technique the graphene remains pristine as it is not exposed to any environmental residue or Poly(methyl methacrylate) (PMMA).

The MC studies were carried out on two graphene superlattice devices. A schematic of the devices is shown in Fig. 1(a), where the conductance of the device is measured between the source and drain using a standard lock-in technique. The carrier concentration was controlled using back-gate voltage V_{BG} for device 1 and using top-gate voltage V_{TG} for device 2. The gate voltage responses of the devices are shown in Figs. 1(b) and 1(c). Along with the resistance peak at the charge neutrality point (CNP) two more resistance peaks are observed symmetrically around the CNP. The resistance peak on the hole side is much stronger than that on the electron side, which is consistent with previous reports [43–51]. The energy separation between the PDC and CDC in device 1 is $\sim$190 meV with a moiré wavelength of $\sim$12 nm, whereas it is $\sim$183 meV with a moiré wavelength of $\sim$12.4 nm in device 2. The mobility around the PDC and CDC was estimated to be $\sim$20 000 and 40 000 cm^2/V s for device 1 and device 2, respectively. A charge inhomogeneity of $n_0 \sim$ 3–5$\times 10^{10}$ cm^{-2} was estimated for both the devices (see Supplemental Material (SM) Sec. SI1 [52]). In the following section we discuss MC at different densities around the PDC and CDC as highlighted by the solid and open symbols in Figs. 1(b) and 1(c). The densities near the PDC and CDC are defined as $\delta n_{PDC} = n - n_{PDC}$ and $\delta n_{CDC} = n - n_{CDC}$, where $n_{PDC} \approx 0$ cm^{-2} for
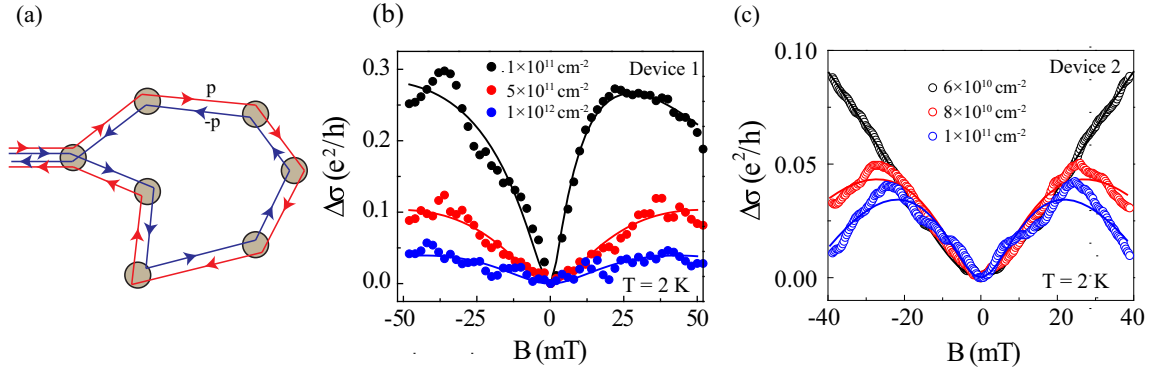
FIG. 2. (a) The schematic of the electron trajectories in the presence of impurities that give rise to quantum correction to conductivity. The magnetoconductance data near CDC at different carrier concentrations δn_{CDC} for (b) device 1 and (c) device 2 at 2 K. The solid curves are the fits to Eq. (1).

device 1 and device 2. On the other hand, n_{CDC}, the location in gate voltage at which the CDC appears, is $\approx 3.1 \times 10^{12}$ and $\approx 3.6 \times 10^{12}$ cm^{-2} for device 1 and device 2, respectively.

III. MAGNETOCONDUCTANCE DATA AT THE CDC

In order to measure the effect of quantum interference on conductivity a small perpendicular magnetic field is applied which introduces an extra phase among the interfering electron wave functions, as shown in Fig. 2(a). As a result, the interference condition changes, and conductance will increase (decrease) with magnetic field for WL (WAL). Figures 2(b) and 2(c) show the change in conductance, $\Delta \sigma(B) = \sigma(B) - \sigma(B = 0)$, with magnetic field at $T = 2$ K for different δn_{CDC} ($5 \times 10^{10} - 1 \times 10^{12}$ cm^{-2}) around the CDC for device 1 and device 2, respectively, as marked by the circles in Fig. 1. In Fig. 3 we show the MC data near the CDC for both devices at different temperatures. The positive nature of the MC in Figs. 2 and 3 suggests the signature of WL around CDC.

The MC in graphene was derived by McCann *et al.* [12],

$$\Delta \sigma(B) = \frac{e^2}{\pi h} \left[F\left(\frac{\tau_B^{-1}}{\tau_\phi^{-1}} \right) - F\left(\frac{\tau_B^{-1}}{\tau_\phi^{-1} + 2\tau_i^{-1}} \right) \right. $$
$$\left. - 2F\left(\frac{\tau_B^{-1}}{\tau_\phi^{-1} + \tau_i^{-1} + \tau_*^{-1}} \right) \right],$$
(1)

where $F(z) = \ln(z) + \psi(\frac{1}{2} + \frac{1}{z})$, ψ is the digamma function, $\tau_B^{-1} = \frac{4eDB}{\hbar}$, τ_ϕ^{-1} is the phase breaking rate, D is the diffusion coefficient, τ_i^{-1} is the intervalley scattering rate, and τ_*^{-1} is the intravalley scattering rate. The main source of intervalley scattering is the short-range scatterers like the edge of the sample or sharp defects, whereas the dislocations, lattice defects, and ripples are the sources of intravalley scattering. In the case of clean sample $\tau_{i,*} \to \infty$, the first two terms in Eq. (1) cancel each other, and the MC is governed by the third term, giving rise to WAL. In the opposite limit of strong intervalley and intravalley scattering (small $\tau_{i,*}$) the last two terms in Eq. (1) are suppressed, and the first term gives WL. The solid lines in Figs. 2(b), 2(c), 3(a), and 3(b) are the theoretical fitting curves of Eq. (1) to extract the different scattering rates as mentioned in SM Sec. SI2 [52].

For small magnetic field Eq. (1) can be reduced to [20]

$$\Delta \sigma(B) = \frac{e^2}{24\pi h} \left(\frac{4eDB\tau_\phi}{\hbar} \right)^2 \left[1 - \frac{1}{(1 + 2\tau_\phi/\tau_i)^2} \right. $$
$$\left. - \frac{2}{(1 + \tau_\phi/\tau_i + \tau_\phi/\tau_*)^2} \right],$$
(2)

and the sign of Eq. (2) determines WL or WAL. The $\Delta \sigma(B) = 0$ curve obtained from Eq. (2) is shown by a solid line in Fig. 3(c) as a function of τ_ϕ/τ_* and τ_ϕ/τ_i. This curve separates the region between WL and WAL. The values of τ_i, τ_*, and τ_ϕ obtained from fitting the MC data at the CDC (Figs. 2 and 3 and SM Sec. SI2 [52]) are used to generate the data points in Fig. 3(c). The error bars in Fig. 3(c) are obtained from the errors in fitting using Eq. (1) in Figs. 2(b), 2(c), 3(a), and 3(b) [52]. It can be clearly seen from Fig. 3(c) that most of the data points are in the WL region for the CDC even for one order variation of temperature and carrier concentration.

It can be seen from Figs. 3(a) and 3(b) that at the CDC the WL becomes weaker with increasing temperature. The behavior with increasing temperature is expected due to the decrement of τ_ϕ (phase coherence length, l_ϕ)[20,53]. With increasing carrier concentration the WL also becomes weaker [Figs. 2(b) and 2(c)]. A similar dependence on carrier concentration was reported in Ref. [53] in graphene due to the enhanced electron-electron scattering rate.

IV. MAGNETOCONDUCTANCE DATA AT PDC

Figure 4 shows MC near the PDC at different temperatures and carrier concentrations for both devices. Although the data are quite symmetric around the zero magnetic field for device 2, there are oscillations at lower carrier concentration as well as lower temperature. One of the possible reasons is universal conductance fluctuations, which have been seen in the literature [21] around the PDC. Because of the oscillating nature of MC we could not fit the data nicely with Eq. (1). Note that the conductance oscillations are much weaker around the CDC in Figs. 2 and 3, and we are able to fit the MC data. Similarly, for device 2, it can be seen from Fig. 4(d) that along with the negative feature of MC around the PDC we also observe a weak feature of positive MC in a very small magnetic field
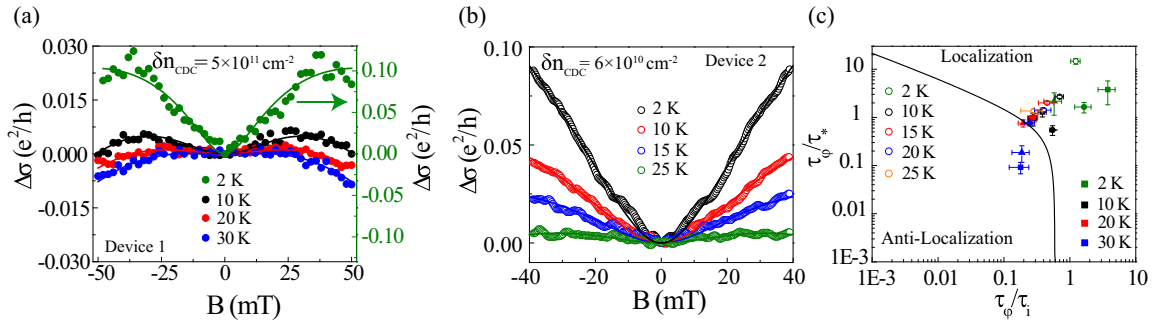
FIG. 3. (a) The magnetoconductance data at different temperatures for $\delta n_{CDC} = 5 \times 10^{11}$ cm^{-2} near CDC for device 1. Note that the ranges of the axis are different for 2 K and other temperatures. (b) The magnetoconductance data at different temperatures for $\delta n_{CDC} = 6 \times 10^{10}$ cm^{-2} near the CDC for device 2. (c) The different scattering times obtained by fitting the experimental data near the CDC for both devices. For device 1, the solid squares, circles, and triangles represent carrier concentrations δn_{CDC} of 1×10^{11}, 5×10^{11}, and 1×10^{12} cm^{-2}, respectively, whereas different colors represent the data for different temperatures. The open symbols represents the data for device 2 at $\delta n_{CDC} = 6 \times 10^{10}$ cm^{-2}. The solid line separates the weak-localization and the weak-antilocalization regions. It can be seen that for both devices the majority of the points near the CDC are in the weak-localization region. The error bars are the fitting errors.

range of ∼10 mT. However, with increasing temperature the weak positive feature of MC vanishes, and a clear negative MC (WAL) emerges, which is consistent with Ref. [20] due to the decrement of the phase coherence length [20,53]. Similarly, with increasing carrier concentration the MC curve at the PDC shows a transition from WAL to WL [Fig. 4(b)], which is also consistent with previous findings [20] due to the increment of intervalley scattering rate. For device 1, the WAL becomes weaker with increasing temperature as well as with carrier concentration. However, from 10 K onwards the MC curves do not show any significant temperature dependence [Fig. 4(c)], suggesting a crossover to the classical regime [54]. The different temperature-dependent MC natures are expected depending on the competition between the different timescales (τ_ϕ, τ_i, τ_*). If τ_i, $\tau_* > \tau_\phi$, MC will exhibit WAL even at the lowest temperature and will be weaker with increasing temperature as τ_ϕ decreases (device 1); in contrast for τ_i, $\tau_* < \tau_\phi$ there can be a crossover with increasing temperature as τ_ϕ decreases, and one can observe the WL to WAL transition as seen in device 2. We note that in both devices the MC curves around the PDC are predominantly negative (WAL) in nature in a certain range of carrier concentration and temperature, in contrast to the strong positive nature of MC (WL) around the CDC in a similar range of carrier concentration and temperature. Note that all the presented MC data were taken at particular gate voltages and not ensemble averaged like in Ref. [55] as the trend of our MC was quite evident.
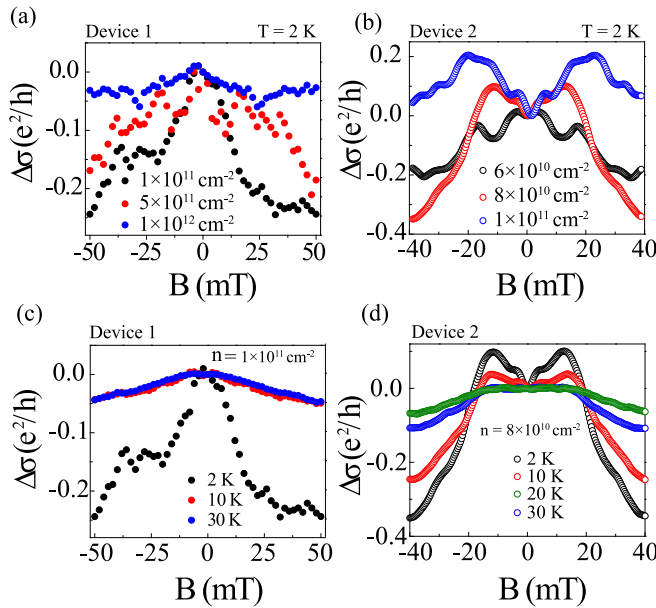
V. QUANTUM OSCILLATION AND BERRY PHASE

WAL was theoretically predicted for cleaner graphene (without intervalley scattering) due to the π Berry phase. In a graphene superlattice with multiple Dirac cones the theory [41] predicts the change in Berry phase from π to 2π (or zero) from the PDC to CDC, which is also verified experimentally [40], and thus, an obvious question is whether the observed positive nature of MC (WL) at the CDC in contrast to the predominantly negative nature of MC (WAL) at the PDC in our GSL devices is due to the Berry phase shift or not. In order to determine the Berry phase we have measured the quantum oscillations in one of our devices.

Figure 5(a) shows the Landau level (LL) spectrum (fan diagram) as a function of magnetic field and gate voltage at $T = 2$ K for device 1. From the conductance data the LLs originating from different Dirac points and their crossing are clearly visible. To calculate the Berry phase we follow the LL maxima or minima originating from the PDC and how it changes after crossing the CDC. The vertical cut lines from Fig. 5(a) are shown at three different gate voltages near the PDC as a function of filling factor, $\nu = nh/4eB$, where n is determined from the PDC. However, due to the limited range of the gate voltage beyond the CDC (because of dielectric breakdown), we just show data for one gate voltage. If we try to plot nearby gate voltages beyond the CDC, the data points will lie on top

FIG. 4. The magnetoconductance data near the PDC at different carrier concentrations δn_{PDC} at 2 K for (a) device 1 and (b) device 2. The magnetoconductance data near the PDC at different temperatures for (c) $\delta n_{PDC} \sim 1 \times 10^{11}$ cm^{-2} for device 1 and (d) for $\delta n_{PDC} \sim 8 \times 10^{10}$ cm^{-2} for device 2.
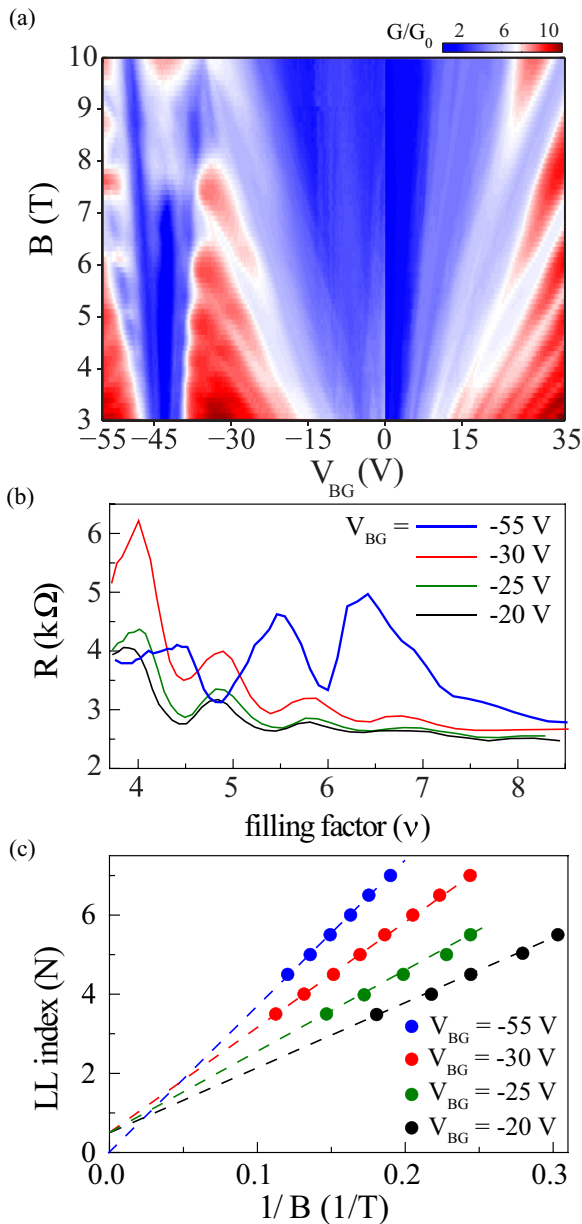
(a)

(b)

(c)

FIG. 5. (a) The Landau fan diagram as a function of magnetic field and gate voltage. Clear LLs can be seen originating from the PDC and CDC (hole side). (b) The resistance as a function of the filling factor, which is obtained from the vertical cut lines of Fig. 5(a) at different gate voltages $V_{BG} = -20, -25, -30,$ and -55 V. (c) The $1/B$ value of the Nth minimum and Nth $+ 1/2$ maximum for the magnetoconductance data shown in (a). The y intercept for data near the PDC for $V_{BG} = -30, -25,$ and -20 V corresponds to $0.45 \pm 0.04, 0.55 \pm 0.12,$ and 0.48 ± 0.13, respectively, whereas the y intercept near the CDC for $V_{BG} = -55$ V corresponds to 0.06 ± 0.04. Two different y intercepts of ∼0.5 and 0 correspond to Berry phases of π and zero (2π) for the PDC and CDC, respectively.

of each other. Thus, for clarity we show only one representative gate voltage beyond the CDC. As can be seen Fig. 5 all the cut lines near the PDC are in phase with each other, and they are out of phase with the CDC data point. Like in Fig. 5(b), the phase shift can also be obtained from an analysis of the fan diagram [Fig. 5(a)] in terms of $1/B$, where the

modulation of the resistance can be written as [56,57] $\Delta R_{xx} = R(B, T) \cos[2\pi(B_F/B + 1/2 + \beta)]$, where $R(B, T)$ is the prefactor, B_F is the frequency of oscillation in $1/B$, and β is the associated Berry phase, in the range $0 < \beta < 1$. Here, $\beta = 0.5$ and 0 correspond to Berry phases of π and 2π (or zero), respectively. We first locate the peaks and valleys of the oscillations in terms of $1/B$ along the vertical dashed lines in Fig. 5(a) and then plot them against their Landau index N, which is shown in Fig. 5(c). The slope of the linear fit gives the oscillation frequency related to carrier concentration, whereas the intercept yields the Berry phase β in units of 2π. From the fitting we determine the Berry phase along with the error bars at various gate voltages. The y-axis intercept varies from 0.45 to 0.55 near the PDC, whereas it is 0.06 near the CDC, indicating a π phase shift between the PDC and CDC. The fitting errors are mentioned in the figure caption. Although the measured Berry phase shift by π may explain the observed WL at the CDC, one needs to understand theoretically why the Berry phase changes in the GSL. In the following section we will try to answer this question by calculating the Berry curvature around the PDC and CDC in the GSL.

VI. THEORETICAL CALCULATIONS

In this section we calculate the Berry phase using realistic band structures. The low-energy electronic structure of the GSL/hBN setup can be modeled within the tight-binding approximation, with its parameters obtained from *ab initio* calculations [58]. The resulting band structure shows cloning of the Dirac cone into six more Dirac cones around the K and K' points. The computed dispersion is schematically shown in the inset of Fig. 1(b). In order to calculate the Berry curvature F, we use the Kubo formula in the two-dimensional momentum space (torus). In the context of graphene and a topological insulator, it is known that the Berry curvature obtains a singular peak if there is a nontrivial band inversion at a single **K** point (or in a nodal ring), as shown in Fig. 6(a). In the presence of time reversal the Berry curvatures at the K and K' points of PDCs are exactly equal but opposite. As the chemical potential is tuned to the CDC, we notice that at each CDC, there occurs an additional band inversion [Fig. 1(b), inset]. Here, the main bands in the reduced moiré BZ and the shadow bands from outside the BZ undergo inversion and produce additional Dirac cones. Although due to weak hBN potential these cones have a finite gap, but owing to the associated band inversion, each gapped CDCs obtains finite Berry curvature. As expected, the Berry curvature at each CDC is finite but opposite in sign, as shown in Fig. 6(b). The net Berry flux or Berry phase of a band can be defined as

$$\gamma_n = \int_{\Omega_{BZ}} dk_x dk_y F^n(\mathbf{k}), \qquad (3)$$

where n is the band index and Ω_{BZ} is the phase-space area of the BZ. The Berry phase will be zero or 2π if the Fermi surface encloses all six K points around the superlattice BZ. The Fermi surface cuts at two representative energies (one below the PDC and the other below the CDC) are shown in Figs. 6(c) and 6(d). The Fermi surface at ∼100 meV below the PDC [Fig. 6(c)] clearly encloses one K point, giving rise to the π Berry phase, whereas the Fermi surface at ∼40 meV below
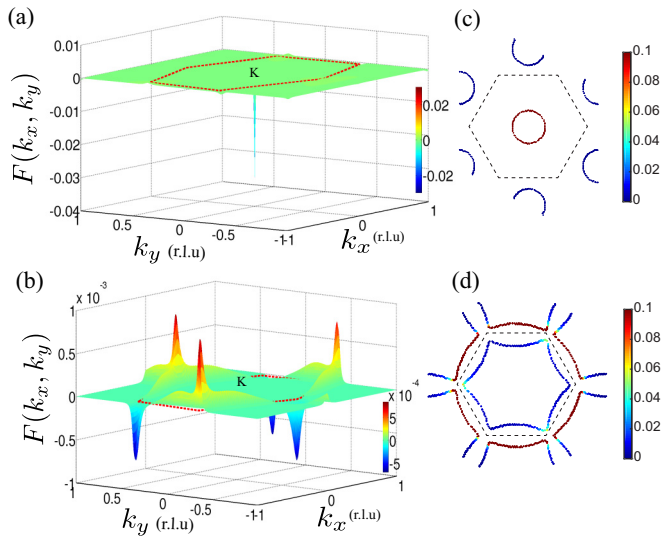
FIG. 6. Berry curvature variation within the moiré superlattice Brillouin zone (BZ; red hexagon). K indicates the Dirac point of graphene. (a) Strong Berry curvature peak at the superlattice BZ center near the PDC. (b) Berry curvature around the CDC within the superlattice BZ showing alternate positive and negative variations (r.l.u = reciprocal lattice unit). (c) The Fermi surface cut at -100 meV from the PDC encloses only one K point. (d) The Fermi surface cut at -40 meV from the CDC. The Fermi surface in the reduced superlattice BZ is shared by all six new K points. The color bar indicates the weightage of the main band and shadow band.

the CDC encloses none of the six K points completely in the reduced BZ, but rather partially captures all six K points, giving rise to the 2π (or zero) Berry phase. The evolution of the Fermi surface while crossing the CDC is shown in the SM Sec. SI3 [52], where one can see that the Fermi surfaces very close to the CDC enclose only one CDC point within ~ 25 meV around the CDC. Thus, the calculated Berry phase will depend on the position of the Fermi energy. However, experimentally observing the π Berry phase close to the CDC is technically challenging due to the presence of electron-hole puddles (more than a few tens of meV) and charge inhomogeneities [25,27,29,30,32]. Experimentally, one can verify the nature of the Fermi surface from the quantum oscillation measurements by estimating the Fermi surface area $S = \frac{2\pi e}{\hbar c \Delta(1/B)}$ from the period $\Delta(1/B)$ of $1/B$ oscillations. In the SM [52] we show the Fermi surface determination at -21 and -29 V below the PDC and at -55 V below the CDC. The experimentally determined Fermi surface area below the PDC matches very well the calculated area from the carrier concentration, $S = \pi k_F{}^2 = \delta n \pi^2$, where $\delta n = \delta n_{\text{PDC}}$. However, below the CDC (-55 V) the Fermi surface area measured from the period of $1/B$ is much higher (four to five

times) than the calculated Fermi surface using $\delta n = \delta n_{\text{CDC}}$ (see SM Sec. SI4 [52]), indicating that the Fermi surface does not enclose only one CDC and thus supports our theoretical Fermi surface calculation in Fig. 6(d).

In the end, it is reasonable to ask whether the Berry phase change from the PDC to CDC is the only possible explanation for observing predominantly WAL around the PDC and WL around the CDC or if there could be some alternative explanations. One of the plausible explanations could be the following: In a GSL, the superlattice Brillouin zone is reduced compared to the pristine Brillouin zone of graphene. Thus, the K and K' valleys at the CDC are connected by a small momentum change compared to the K and K' valleys at the PDC, and hence, GSL is expected to have more intervalley scattering at the CDC than at the PDC without the requirement of any Berry phase change and thus can explain the WAL at the PDC and WL at the CDC. The shift of the Berry phase will enhance the effect (intervalley scattering) at the CDC more significantly since the backscattering protection is lifted as a consequence of the 2π (or zero) Berry phase. However, it is very difficult to find their (small momentum change vs Berry phase change) relative contributions to WL at the CDC in a GSL device. Nevertheless, from our Fermi surface determination and theoretical calculation it is clear that the Fermi surface partially encloses all six K points around the CDC [Fig. 6(d)]; thus, the valleys are not isolated from each other, rendering the distinction between intervalley and intravalley scatterings ill defined. Therefore, we believe the total Berry phase of 2π (or zero) is the main cause of the observed WL around the CDC.

VII. CONCLUSION

In conclusion, we have carried out magnetoconductance studies in GSL devices. Our MC data show a clear signature of positive nature (WL) at the CDC over one order variation of carrier concentration and temperature, whereas the nature is predominately negative (WAL) at lower carrier concentration as well as a certain temperature range. We also measured the quantum oscillations in a GSL device showing the shift of Berry phase from π at the PDC to 2π (or zero) at the CDC. These two experimental observations with theoretical support suggest the effect of Berry phase on localization physics. These studies will help to understand the quantum corrections to the conductivity at multiple Dirac cones in graphene super-lattices and will also stimulate further theoretical studies on localization physics in a graphene superlattice.

[1] B. L. Altshuler, D. Khmel'nitzkii, A. I. Larkin, and P. A. Lee, Phys. Rev. B **22**, 5142 (1980).

[2] G. Bergmann, Phys. Rep. **107**, 1 (1984).

[3] J. C. Licini, G. J. Dolan, and D. J. Bishop, Phys. Rev. Lett. **54**, 1585 (1985).

[4] A. Savchenko, A. Rylik, and V. Lutskii, Zh. Eksp. Teor. Fiz. **85**, 2210 (1983).

[5] C. Schierholz, R. Kürsten, G. Meier, T. Matsuyama, and U. Merkt, Phys. Status Solidi B **233**, 436 (2002).

[6] J. B. Miller, D. M. Zumbühl, C. M. Marcus, Y. B. Lyanda-Geller, D. Goldhaber-Gordon, K. Campman, and A. C. Gossard, Phys. Rev. Lett. **90**, 076807 (2003).

[7] T. Nihei, Y. Suzuki, M. Kohda, and J. Nitta, Phys. Status Solidi C **3**, 4239 (2006).

[8] I. P. Smorchkova, N. Samarth, J. M. Kikkawa, and D. D. Awschalom, Phys. Rev. Lett. **78**, 3571 (1997).

[9] B. Grbić, R. Leturcq, T. Ihn, K. Ensslin, D. Reuter, and A. D. Wieck, Phys. Rev. B **77**, 125312 (2008).

[10] T. Ando, T. Nakanishi, and R. Saito, J. Phys. Soc. Jpn. **67**, 2857 (1998).

[11] H. Suzuura and T. Ando, Phys. Rev. Lett. **89**, 266603 (2002).

[12] E. McCann, K. Kechedzhi, V. I. Fal'ko, H. Suzuura, T. Ando, and B. L. Altshuler, Phys. Rev. Lett. **97**, 146805 (2006).

[13] K. Nomura and A. H. MacDonald, Phys. Rev. Lett. **98**, 076602 (2007).

[14] A. F. Morpurgo and F. Guinea, Phys. Rev. Lett. **97**, 196804 (2006).

[15] K. Kechedzhi, V. I. Fal'ko, E. McCann, and B. L. Altshuler, Phys. Rev. Lett. **98**, 176806 (2007).

[16] D. V. Khveshchenko, Phys. Rev. Lett. **97**, 036802 (2006).

[17] S. V. Morozov, K. S. Novoselov, M. I. Katsnelson, F. Schedin, L. A. Ponomarenko, D. Jiang, and A. K. Geim, Phys. Rev. Lett. **97**, 016801 (2006).

[18] H. B. Heersche, P. Jarillo-Herrero, J. B. Oostinga, L. M. Vandersypen, and A. F. Morpurgo, Nature **446**, 56 (2007).

[19] C. Berger, Z. Song, X. Li, X. Wu, N. Brown, C. Naud, D. Mayou, T. Li, and Hass, Science **312**, 1191 (2006).

[20] F. V. Tikhonenko, A. A. Kozikov, A. K. Savchenko, and R. V. Gorbachev, Phys. Rev. Lett. **103**, 226801 (2009).

[21] J. Berezovsky and R. M. Westervelt, Nanotechnology **21**, 274014 (2010).

[22] Y.-F. Chen, M.-H. Bae, C. Chialvo, T. Dirks, A. Bezryadin, and N. Mason, J. Phys.: Condens. Matter **22**, 205301 (2010).

[23] A. M. R. Baker, J. A. Alexander-Webber, T. Altebaeumer, T. J. B. M. Janssen, A. Tzalenchuk, S. Lara-Avila, S. Kubatkin, R. Yakimova, C.-T. Lin, L.-J. Li, and R. J. Nicholas, Phys. Rev. B **86**, 235441 (2012).

[24] A. Mahmood, C. Naud, C. Bouvier, F. Hiebel, P. Mallet, J.-Y. Veuillen, L. Lévy, D. Chaussende, and T. Ouisse, J. Appl. Phys. **113**, 083715 (2013).

[25] M. Iqbal, Ö. Kelekçi, M. Iqbal, X. Jin, C. Hwang, and J. Eom, New J. Phys. **16**, 083020 (2014).

[26] M. Hilke, M. Massicotte, E. Whiteway, and V. Yu, Sci. World J. **2014**, 8 (2014).

[27] U. Chandni, E. A. Henriksen, and J. P. Eisenstein, Phys. Rev. B **91**, 245402 (2015).

[28] A. N. Pal, V. Kochat, and A. Ghosh, Phys. Rev. Lett. **109**, 196601 (2012).

[29] D.-K. Ki, D. Jeong, J.-H. Choi, H.-J. Lee, and K.-S. Park, Phys. Rev. B **78**, 125409 (2008).

[30] F. V. Tikhonenko, D. W. Horsell, R. V. Gorbachev, and A. K. Savchenko, Phys. Rev. Lett. **100**, 056802 (2008).

[31] Y. Oh, J. Eom, H. C. Koo, and S. H. Han, Solid State Commun. **150**, 1987 (2010).

[32] J. Moser, H. Tao, S. Roche, F. Alzina, C. M. Sotomayor Torres, and A. Bachtold, Phys. Rev. B **81**, 205445 (2010).

[33] M. B. Lundeberg and J. A. Folk, Phys. Rev. Lett. **105**, 146804 (2010).

[34] X. Wu, X. Li, Z. Song, C. Berger, and W. A. de Heer, Phys. Rev. Lett. **98**, 136801 (2007).

[35] Y. Liu, W. S. Lew, and L. Sun, Phys. Chem. Chem. Phys. **13**, 20208 (2011).

[36] B. Jouault, B. Jabakhanji, N. Camara, W. Desrat, C. Consejo, and J. Camassel, Phys. Rev. B **83**, 195417 (2011).

[37] V. I. Fal'ko, K. Kechedzhi, E. McCann, B. Altshuler, H. Suzuura, and T. Ando, Solid State Commun. **143**, 33 (2007).

[38] Y.-F. Chen, M.-H. Bae, C. Chialvo, T. Dirks, A. Bezryadin, and N. Mason, Physica B (Amsterdam, Neth.) **406**, 785 (2011).

[39] I. L. Aleiner and K. B. Efetov, Phys. Rev. Lett. **97**, 236801 (2006).

[40] P. Wang, B. Cheng, O. Martynov, T. Miao, L. Jing, T. Taniguchi, K. Watanabe, V. Aji, C. N. Lau, and M. Bockrath, Nano Lett. **15**, 6395 (2015).

[41] J. C. Song, P. Samutpraphoot, and L. S. Levitov, Proc. Natl. Acad. Sci. USA **112**, 10879 (2015).

[42] P. Zomer, S. Dash, N. Tombros, and B. Van Wees, Appl. Phys. Lett. **99**, 232104 (2011).

[43] M. Yankowitz, J. Xue, D. Cormode, J. D. Sanchez-Yamagishi, K. Watanabe, T. Taniguchi, P. Jarillo-Herrero, P. Jacquod, and B. J. LeRoy, Nat. Phys. **8**, 382 (2012).

[44] B. Hunt, J. Sanchez-Yamagishi, A. Young, M. Yankowitz, B. J. LeRoy, K. Watanabe, T. Taniguchi, P. Moon, M. Koshino, and P. Jarillo-Herrero, Science **340**, 1427 (2013).

[45] C. Dean, L. Wang, P. Maher, C. Forsythe, F. Ghahari, Y. Gao, J. Katoch, M. Ishigami, P. Moon, and M. Koshino, Nature **497**, 598 (2013).

[46] L. Ponomarenko, R. Gorbachev, G. Yu, D. Elias, R. Jalil, A. Patel, A. Mishchenko, A. Mayorov, C. Woods, and Wallbank, Nature (London) **497**, 594 (2013).

[47] G. Yu, R. Gorbachev, J. Tu, A. Kretinin, Y. Cao, R. Jalil, F. Withers, L. Ponomarenko, B. Piot, and M. Potemski, Nat. Phys. **10**, 525 (2014).

[48] C. Woods, L. Britnell, A. Eckmann, R. Ma, J. Lu, H. Guo, X. Lin, G. Yu, Y. Cao, and R. Gorbachev, Nat. Phys. **10**, 451 (2014).

[49] R. Gorbachev, J. Song, G. Yu, A. Kretinin, F. Withers, Y. Cao, A. Mishchenko, I. Grigorieva, K. Novoselov, and L. Levitov, Science **346**, 448 (2014).

[50] L. Wang, Y. Gao, B. Wen, Z. Han, T. Taniguchi, K. Watanabe, M. Koshino, J. Hone, and C. R. Dean, Science **350**, 1231 (2015).

[51] C. Kumar, M. Kuiri, J. Jung, T. Das, and A. Das, Nano Lett. **16**, 1042 (2016).

[52] See Supplemental Material at http://link.aps.org/supplemental/10.1103/PhysRevB.98.155408 for additional data on device fabrication and characterization, magnetoconductance data at the PDC and CDC, the calculation of different scattering rates, the dephasing mechanism, the density of states, Fermi surface calculations, and the estimation of the Fermi surface from quantum oscillation.

[53] S. Pezzini, C. Cobaleda, E. Diez, and V. Bellani, Phys. Rev. B **85**, 165451 (2012).

[54] Z. Wang, D.-K. Ki, J. Y. Khoo, D. Mauro, H. Berger, L. S. Levitov, and A. F. Morpurgo, Phys. Rev. X **6**, 041020 (2016).

[55] Z. Wang, D.-K. Ki, H. Chen, H. Berger, A. H. MacDonald, and A. F. Morpurgo, Nat. Commun. **6**, 8339 (2015).

[56] Y. Zhang, Y.-W. Tan, H. L. Stormer, and P. Kim, Nature (London) **438**, 201 (2005).

[57] K. S. Novoselov, A. K. Geim, S. Morozov, D. Jiang, M. Katsnelson, I. Grigorieva, S. Dubonos, and A. Firsov, Nature (London) **438**, 197 (2005).

[58] J. Jung, A. Raoux, Z. Qiao, and A. H. MacDonald, Phys. Rev. B **89**, 205414 (2014).